Exploring Non-Local Spatial-Angular Correlations with a Hybrid Mamba-Transformer Framework for Light Field Super-Resolution

Haosong Liu, *Graduate Student Member, IEEE*, Xiancheng Zhu, *Graduate Student Member, IEEE*, Huanqiang Zeng, *Senior Member, IEEE*, Jianqing Zhu, *Senior Member, IEEE*, Jiuwen Cao, *Senior Member, IEEE* and Junhui Hou, *Senior Member, IEEE*

***Abstract*—Recently, Mamba-based methods, with its advantage in long-range information modeling and linear complexity, have shown great potential in optimizing both computational cost and performance of light field image super-resolution (LFSR). However, current multi-directional scanning strategies lead to inefficient and redundant feature extraction when applied to complex LF data. To overcome this challenge, we propose a Subspace Simple Scanning (Sub-SS) strategy, based on which we design the Subspace Simple Mamba Block (SSMB) to achieve more efficient and precise feature extraction. Furthermore, we propose a dual-stage modeling strategy to address the limitation of state space in preserving spatial-angular and disparity information, thereby enabling a more comprehensive exploration of non-local spatial-angular correlations. Specifically, in stage I, we introduce the Spatial-Angular Residual Subspace Mamba Block (SA-RSMB) for shallow spatial-angular feature extraction; in stage II, we use a dual-branch parallel structure combining the Epipolar Plane Mamba Block (EPMB) and Epipolar Plane Transformer Block (EPTB) for deep epipolar feature refinement. Building upon meticulously designed modules and strategies, we introduce a hybrid Mamba-Transformer framework, termed LFMT. LFMT integrates the strengths of Mamba and Transformer models for LFSR, enabling comprehensive information exploration across spatial, angular, and epipolar-plane domains. Experimental results demonstrate that LFMT significantly outperforms current state-of-the-art methods in LFSR, achieving substantial improvements in performance while maintaining low computational complexity on both real-word and synthetic LF datasets. The code is available at https://github.com/hsliu01/LFMT.**

This work was supported in part by the Key Science and Technology Project of Fujian Province under Grant 2024HZ022007, in part by the Key Program of Natural Science Foundation of Fujian Province under Grant 2023J02022, in part by the Natural Science Foundation for Outstanding Young Scholars of Fujian Province under Grant 2022J06023, in part by the Natural Science Foundation of Fujian Province under Grant 2022J01294, in part by the Natural Science Foundation of Zhejiang Province under Grant LZ24F030010, and in part by the High-level Talent Team Project of Quanzhou City under Grant 2023CT001 (*Corresponding author: Huanqiang Zeng*).

Haosong Liu is with the School of Information Science and Engineering, Huaqiao University, Xiamen 361021, China (e-mail: hsliu@stu.hqu.edu.cn).

Xiancheng Zhu is with the School of Mechanical Engineering and Automation, Huaqiao University, Xiamen 361021, China (e-mail: xianchengzhu@stu.hqu.edu.cn).

Huanqiang Zeng is with the School of Engineering, Huaqiao University, Quanzhou 362021, China, and also with the School of Optoelectronic and Communication Engineering, Xiamen University of Technology, Xiamen 361024, China (e-mail: zeng0043@hqu.edu.cn).

Jianqing Zhu is with the School of Engineering, Huaqiao University, Quanzhou 362021, China (e-mail: jqzhu@hqu.edu.cn).

Jiuwen Cao is with the Artificial Intelligence Institute, Hangzhou Dianzi University, Hangzhou 310018, China (e-mail: jwcao@hdu.edu.cn).

Junhui Hou is with the Department of Computer Science, City University of Hong Kong, Hong Kong (e-mail: jh.hou@cityu.edu.hk).

Haosong Liu and Xiancheng Zhu contributed equally to this work.

***Index Terms*—Light field, super-resolution, state space model, mamba.**

I. Introduction

LIGHT Fields (LFs) capture both the intensities (spatial information) and directions (angular information) of light rays, providing richer information than traditional images [1]. In recent years, the rise of portable LF cameras, such as Lytro and Raytrix, has accelerated the application of LF images, demonstrating great potential in areas such as post-capture refocusing [2], [3], depth estimation [4]–[8], 3D reconstruction [9], and virtual reality [10], [11]. However, despite enhancing angular resolution through microlens arrays, these cameras inevitably compromise spatial resolution [1], thereby restricting their practical applicability. Therefore, LFSR algorithms have been widely studied to improve the spatial resolution of LF images.

In recent years, Convolutional Neural Networks (CNNs) have been widely applied to LFSR, aiming to learn complex spatial-angular information or correlations within LF images. A variety of feature extraction strategies have been proposed to alleviate the spatial-angular entanglement in 4D LF images. Some methods [12]–[20] extract features through several convolutions in single subspace to learn spatial or angular information, while others [21]–[28] utilize combined convolutions across multiple subspaces to extract and fuse features, thereby learning spatial-angular correlations. However, these methods fail to fully leverage the complete information in all subspaces, and the local receptive field of CNNs restricts the interaction in individual subspace or across different subspaces, resulting in inadequate exploration of spatial-angular correlations.

Transformer models, known for their ability to capture long-range dependencies, have been increasingly applied to LFSR. Enhancing long-range interactions improves the modeling of non-local spatial-angular correlations. For example, networks such as LFT [29], DPT [30] and LF-DET [31] extract long-range information from spatial and angular domains, while EPIT [32] alternately extract the horizontal and vertical structural information from epipolar plane domain. However, due to the quadratic complexity of self-attention computation, Transformer-based methods face challenges in constructing deeper networks to extract high-frequency information in all domains. This limitation hinders their ability to effectively and comprehensively explore non-local spatial-angular correlations in LF images. Therefore, effectively utilizing the complete

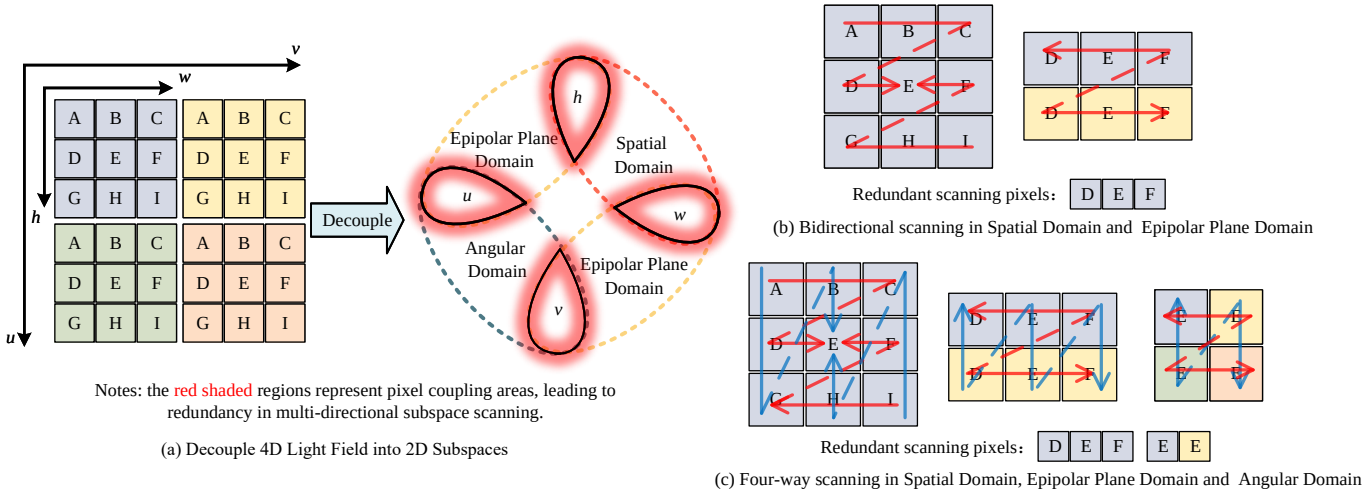

Notes: the red shaded regions represent pixel coupling areas, leading to redundancy in multi-directional subspace scanning.

(a) Decouple 4D Light Field into 2D Subspaces

(b) Bidirectional scanning in Spatial Domain and Epipolar Plane Domain

(c) Four-way scanning in Spatial Domain, Epipolar Plane Domain and Angular Domain

Fig. 1. (a) The 4D LF can be decoupled into 2D subspaces, including the spatial, angular, and epipolar plane domains. For illustration, the LF images on the left is shown with $u = v = 2$ and $h = w = 3$, where different colors represent different viewpoints, and different letters indicate different pixels in the same viewpoint. (b) The coupling in bidirectional scanning [36]: when bidirectional scanning is performed in spatial and epipolar plane domains, the correlations between blue pixels D, E, F are redundantly modeled. (c) The coupling in four-way scanning [37]: when four-way scanning is performed in spatial, angular, and epipolar plane domains, the correlations between blue pixels D, E, F, as well as between blue pixel E, yellow pixel E, are redundantly modeled.

information in all domains to model non-local spatial-angular correlations remains a significant challenge.

Recently, State Space Models (SSMs), particularly Mamba [33], have emerged as a powerful competitor to Transformer models, maintaining linear computational complexity while enabling long-range information modeling. Pure Mamba-based methods (e.g., MLFSR [34] and LFMamba [35]) adopt the multi-directional scanning strategy to model non-local spatial-angular correlations. However, they overlook the inherent complexity and redundancy of LF data, resulting in limited efficiency and insufficient capability to capture the fine-grained spatial-angular structures required for high-fidelity LFSR. In contrast, pure Transformer models excel at global context modeling and can better restore spatial-angular structures close to the original LF. Nevertheless, their reliance on unfolding 4D LF data into 1D sequences for modeling incurs prohibitive computational costs, thereby constraining overall performance. As illustrated in Fig. 1(b) and Fig. 1(c), the coupling of LF subspace scanning may lead to computational redundancy and degrade performance in modeling non-local spatial–angular correlations. To overcome this challenge, we design the Subspace Simple Mamba Block (SSMB) as a basic component for feature extraction in LF subspaces, which adopts the Subspace Simple Scanning (Sub-SS) strategy to mitigate the inefficiency and coupling (refer to Sec. III-C for details). Additionally, to further enhance the utilization of feature space information, we introduce a symmetric branch composed of convolution and SiLU activation to compensate for the information loss caused by the Sub-SS sequential constraints.

Furthermore, when the sequence length is excessively long, the limited state space may fail to adequately preserve spatial-angular and disparity information, thereby hindering the deeper exploration of spatial-angular correlations. To tackle this challenge, we propose a dual-stage modeling strategy to capture non-local spatial-angular correlations. Specifically, in Stage I, we focus on the coarse extraction of shallow spatial-angular features from spatial and angular domains. We first construct the Residual Subspace Mamba Block (RSMB) to reduce channel redundancy and achieve more efficient nonlocal feature aggregation. Subsequently, we design the Spatial-Angular Residual Subspace Mamba Block (SA-RSMB), where the RSMB is ingeniously applied in the alternating processing of the spatial and angular domains to capture non-local spatial and angular feature. In Stage II, we thoroughly explore the deep interaction between LF disparity and structural information in epipolar plane domain for deep epipolar feature refinement. Building on the design strategy of SA-RSMB, we introduce the Epipolar Plane Mamba Block (EPMB) to extract disparity and structural information from epipolar plane domain, further refining the spatial-angular feature.

The epipolar plane domain deeply couples spatial and angular information, as shown in Fig. 1(a). This information reflects the intrinsic structure of LF and contributes to promoting the refinement and enhancement of non-local spatial-angular correlations. Although EPMB demonstrates efficient long-range dependency modeling, its limited state space restricts deeper feature understanding, which may obstruct the capture of structural information in epipolar plane domain. To address this, we introduce the LFMT network that combines the strengths of Mamba and Transformer models for the first time. Specifically, we adopt a dual branch parallel structure, introducing a few Epipolar Plane Transformer Blocks (EPTB) with quadratic computational complexity in Stage II. This strategy compensates for the limitation of EPMB in enhancing spatial-angular correlations, enabling a more comprehensive exploration of deep disparity and structural information.

We conduct extensive ablation experiments on real-world and synthetic LF datasets, validating the superior performance of LFMT in LFSR. Our contributions are summarized as follows:

- We propose a Sub-SS strategy and construct the SSMB, which addresses the issue of inefficient feature extraction

caused by the coupling of LF subspace scanning in LFSR.
- We propose a dual-stage strategy for modeling non-local spatial-angular correlations that effectively preserves spatial-angular and disparity information.
- We propose the LFMT network, which combines the advantages of Mamba and Transformer models for LFSR. LFMT accomplishes non-local spatial-angular correlations modeling from coarse to fine through complete information interaction in all 2D subspaces.
- Experimental results confirm that our method achieves new state-of-the-art performance in LFSR both quantitatively and qualitatively, while maintaining low computational complexity.

II. Relate Work

A. Light Field 2D Subspace Representation

LFs are commonly represented in 4D using the two-plane parameterization model $L(u, v, h, w)$ proposed by Levoy et al. [38], where (u, v) represents the viewpoint plane, and (h, w) represents the image plane. However, the spatial and angular information in the complex and voluminous 4D LF data are highly coupled, making the modeling of spatial-angular correlations challenging. A common approach is to project 4D LF data into 2D subspaces, as shown in Fig. 2. The primary types of 2D subspace representations include sub-aperture images (SAIs), macro-pixel images (MacPIs), and epipolar-plane images (EPIs), respectively corresponding to the spatial, angular, and epipolar-plane domains. The epipolar-plane domain bridges the spatial and angular domains, encoding spatial-angular information. Notably, EPIs reflect disparity values through slanted line patterns, enabling the exploration of deeper disparity and structural information.

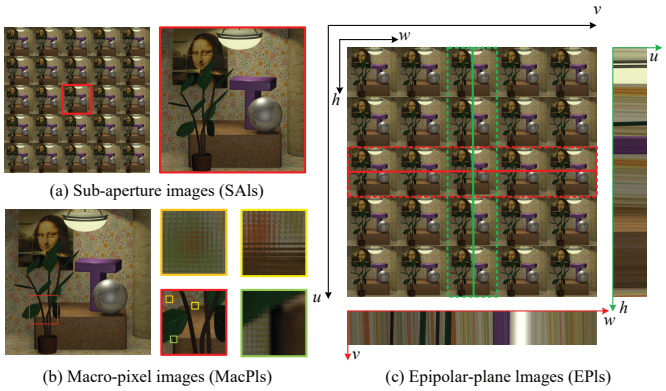

(a) Sub-aperture images (SAIs)

(b) Macro-pixel images (MacPIs)

(c) Epipolar-plane Images (EPIs)

Fig. 2. The projection of 4D LF data into 2D subspaces: (a) SAI pattern projected into the spatial domain, (b) MacPI pattern projected into the angular domain, and (c) EPI pattern projected into the epipolar plane domain.

B. Light Field Image Super-Resolution

The task of LFSR typically aims to enhance the spatial resolution of each sub-aperture image. As LF images become increasingly adopted in various applications, this technology has received considerable attention in recent years. By utilizing advancements in modern neural networks, LFSR has made significant breakthroughs. Currently, mainstream deep learning-based methods for LFSR can be broadly categorized into two types: CNN-based methods and Transformer-based methods.

To address the challenges in spatial-angular feature modeling for LFSR, various CNN-based methods have been proposed with progressive improvements. Yoon *et al.* [12] first introduced LFCNN, pioneering the use of CNNs to explore correlations between adjacent SAIs and achieving joint spatial-angular super-resolution. Building upon this, Zhang *et al.* [13] proposed resLF, which groups SAIs with consistent sub-pixel disparities into stacks and employs residual convolutions to extract epipolar features more effectively. To further enhance spatial-angular interaction, Yeung *et al.* [14] introduced 4D convolutions and spatial-angular separated convolutions to model complex structural dependencies in both domains. Jin *et al.* [15] presented the "All-to-One" model, integrating complementary information across multiple viewpoints while preserving the disparity structure of LF images. Extending the separation and fusion paradigm, Wang *et al.* [39] developed LF-InterNet, which extracts spatial and angular features independently and fuses them via feature interaction modules. This design was further improved in DistgSSR [40], which introduces a decoupling mechanism based on convolutions with varying dilation rates to more flexibly capture spatial-angular correlations. The works of Hou *et al.* [41]–[43] make significant contributions to LFSR by introducing complementary strategies such as view synthesis, coded-aperture camera reconstruction, and regularized feature learning, which enhance the recovery of both spatial and angular information in a more comprehensive manner. To robustly handle diverse real-world degradations, Xiao *et al.* [44] proposed LF-DEST, a blind LFSR method that integrates explicit degradation estimation with a modulated selective fusion module. More recently, Van *et al.* [28] proposed HLFSR, which decomposes the 4D LF into multiple 2D subspaces to enable efficient feature extraction and attention-based fusion. Despite their evolution from early pairwise SAI modeling to advanced exploitation of epipolar geometry and subspace decomposition, CNN-based methods remain constrained by limited receptive fields, hindering effective modeling of non-local spatial-angular correlations.

Recent studies have introduced Transformer-based methods into LFSR to solve the problem of global information interaction. The main idea of these methods is to transform pixels into sequences and approach LFSR as a sequence-to-sequence reconstruction task. By the self-attention mechanism, these methods can learn non-local spatial-angular correlations and model long-range dependency across the spatial and angular domains. Liang *et al.* [29] first proposed LFT and utilised Transformer-based architecture to alternately extract long-range feature in spatial and angular domains, achieving non-local spatial-angular information interaction. Wang *et al.* [30] introduced the detail-preserving transformer, which flattens vertical or horizontal SAIs and employs LF gradient maps to guide sequence learning, thereby effectively enhancing detail restoration. Liang *et al.* [32] further developed EPIT, a robust network for the large disparity LF scenes. They input vertical

and horizontal EPI pixels as sequences and leveraged basic transformer to learn non-local spatial-angular correlations. Cong *et al.* [31] proposed LF-DET, which applies subsampling convolution layers in spatial domain for sequence mapping and adopts a multi-scale angular modeling strategy in angular domain, achieving more efficient information processing. Xiao *et al.* [45] proposed OHT, a hybrid network that combines convolution and Transformer modules with occlusion-aware spatial-angular modeling to efficiently capture local and global correlations. However, Transformer-based methods face the quadratic computational complexity. This leads to challenges in efficiently applying transformer blocks in all 2D subspaces and in constructing deep networks to extract high-frequency information. Beyond network architecture design, Xiao *et al.* [46] introduced CutMIB, a novel data augmentation strategy for LFSR that leverages implicit geometric cues via multi-view patch blending to enhance reconstruction accuracy and angular consistency.

C. State Space Model

SSMs originate from classical control theory [47] and have recently emerged as a promising architecture in deep learning for long-range dependency modeling. SSMs capture long-range dependency through linear recurrence processes with a computational complexity of $O(N)$, offering a significant advantage over the $O(N^2)$ complexity of Transformer-based methods. S4 [48] introduced a novel parameterization method for structured state spaces, significantly improving the efficiency of long sequence modeling. Building on this, S5 [49] further enhanced long sequence processing capabilities through the multi-input multi-output mechanism and efficient parallel scanning. The H3 model [50] narrowed the performance gap between SSMs and Transformer in natural language tasks, demonstrating the huge potential of SSMs in various applications. In particular, Mamba [33] introduced a selective mechanism that adaptively learns structured parameters from input data, greatly enhancing the model's performance.

Mamba-based methods have been rapidly applied to vision tasks due to their strengths in linear scalability, computational efficiency, and flexibility. The initial studies, including Vim [36] and VMamba [37], employed multi-directional scanning to overcome the causality limitations of Mamba. These works have inspired the application of Mamba in a range of vision tasks, including image segmentation [51], image restoration *et al.*, video understanding [52], [53] and 3D point cloud processing [54], [55]. Mamba's unique strengths in long-range dependency modeling and computational efficiency establish it as a promising method for LFSR. Specifically, Gao *et al.* [34] introduced bidirectional scanning with Mamba for LFSR. Xia *et al.* [35] proposed four-directional scanning along the channel dimension to reduce the excessive number of parameters of Mamba for LFSR task. Additionally, Jin *et al.* [56] proposed the LFTransMamba that integrates Mamba and Transformer, combined with masked LF image modeling and an enhanced position-sensitive window mechanism, to balance spatial–angular consistency modeling and computational complexity. However, pure Mamba-based methods suffer from the coupling of 2D subspace scanning in LF, where pixels are redundantly modeled across subspaces, thus constraining performance. In this work, we further exploit the potential of Mamba for LFSR by introducing a hybrid Mamba-Transformer architecture, which enables comprehensive information interaction across all 2D subspaces and facilitates non-local spatial-angular correlation modeling in a coarse-to-fine manner.

III. Method

A. Mamba Preliminaries

SSMs are the mathematical framework widely used in time series analysis and control systems. They describe the evolution of the system's hidden states and internal dynamic relationships through state equations. The core idea is to establish relationships between the input sequence $x(t) \in \mathbb{R}^L$ and the output sequence $y(t) \in \mathbb{R}^L$ through intermediate hidden states $h(t) \in \mathbb{R}^L$, which capture the underlying structure and dynamic properties of the system. This process is typically represented by linear ordinary differential equations :

$$\begin{aligned} h'(t) &= \mathbf{A}h(t) + \mathbf{B}x(t), \\ y(t) &= \mathbf{C}h(t), \end{aligned} \tag{1}$$

where L is the length of the input sequence, $\mathbf{A} \in \mathbb{R}^{N\times N}$ is the state matrix, $\mathbf{B} \in \mathbb{R}^{N\times 1}$, and $\mathbf{C} \in \mathbb{R}^{N\times 1}$ are projection parameters.

In recent years, for adapt to the training of deep neural networks, the structured state space sequence model (S4) [48] has introduced a timescale parameter Δ to discretize the process in Eq. (1). They use the zero-order hold rule to convert continuous parameters $\mathbf{A}$ and $\mathbf{B}$ into discrete parameters $\overline{\mathbf{A}}$ and $\overline{\mathbf{B}}$:

$$\begin{aligned} \overline{\mathbf{A}} &= \exp(\Delta\mathbf{A}), \\ \overline{\mathbf{B}} &= (\Delta\mathbf{A})^{-1}(\exp(\Delta\mathbf{A}) - \mathbf{I}) \cdot (\Delta\mathbf{B}). \end{aligned} \tag{2}$$

Thus, Eq. (1) is derived into its discrete form:

$$\begin{aligned} h_k &= \overline{\mathbf{A}}h_{k-1} + \overline{\mathbf{B}}x_k, \\ y_k &= \mathbf{C}h_k. \end{aligned} \tag{3}$$

Further, the recursive form of Eq. (3) can be converted into a fast parallel training structure with the structured convolution kernel $\overline{\mathbf{K}} \in \mathbb{R}^L$:

$$\begin{aligned} \overline{\mathbf{K}} &= (\mathbf{C}\overline{\mathbf{B}}, \mathbf{C}\overline{\mathbf{A}\mathbf{B}}, \ldots, \mathbf{C}\overline{\mathbf{A}}^{L-1}\overline{\mathbf{B}}), \\ y &= x * \overline{\mathbf{K}}, \end{aligned} \tag{4}$$

where $*$ denotes the convolution operation.

It bears mentioning that Mamba [33] introduces a context-aware information selection mechanism on the parameters $\overline{\mathbf{B}}$ and $\mathbf{C}$ and proposes a parallel scanning algorithm to accelerate training. This approach achieves weight allocation related to the input and maintains linear computational complexity at the same time, significantly enhancing the efficiency and performance of SSMs.

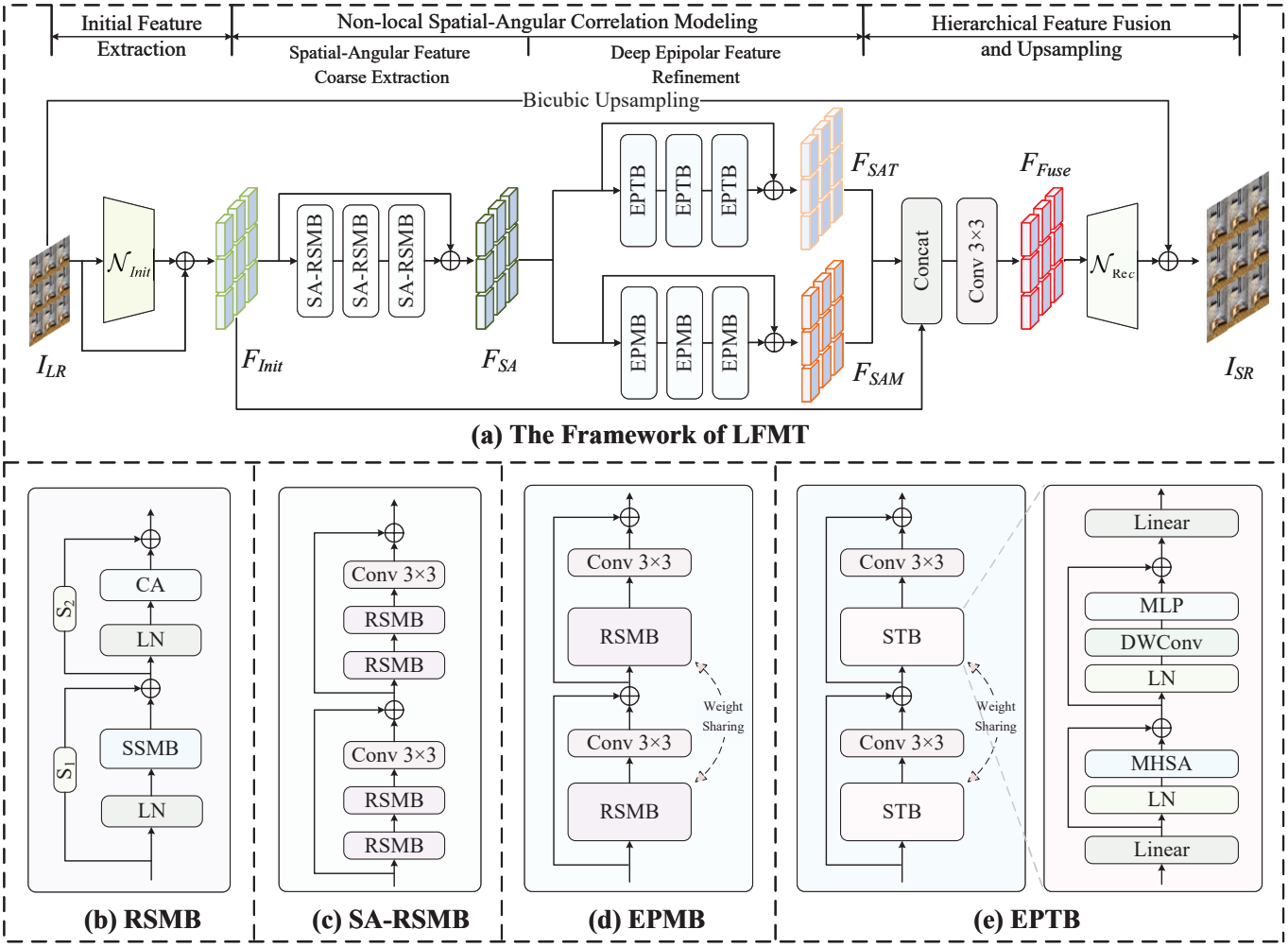

Fig. 3. (a) The overall architecture of the proposed LFMT network. (b) RSMB is used for effective long-range dependency modeling. (c) SA-RSMB is used for shallow spatial-angular feature coarse extraction in spatial and angular domains. (d) EPMB and (e) EPTB are used for deep refinement and enhancement of spatial-angular feature in epipolar plane domain.

B. Overview of LFMT

For the LFSR task, given a low-resolution LF image $I_{LR} \in \mathbb{R}^{U\times V\times H\times W}$, the goal is to reconstruct a high-resolution LF image $I_{HR} \in \mathbb{R}^{U\times V\times \alpha H\times \alpha W}$, where $U \times V$ is the angular resolution, $H \times W$ is the spatial resolution and α is the scale factor. As shown in Fig. 3(a), the LFMT consists of three parts: initial feature extraction, non-local spatial-angular correlations modeling, as well as hierarchical feature fusion and upsampling. Similar to previous works [29], [32], we first use an encoder $\mathcal{N}_{Init}$, composed of cascaded convolutionals, to extract initial features $F_{Init} \in \mathbb{R}^{U\times V\times H\times W\times C}$ from the input I_{LR}, where $C = 64$ is the channel dimension. Then, F_{Init} undergoes a dual-stage spatial-angular correlations modeling from coarse-grained to fine-grained, to accomplish non-local information interaction in all subspaces. Specifically, in Stage I, F_{Init} will be processed by three cascaded SA-RSMBs to extract spatial-angular features $F_{SA} \in \mathbb{R}^{U\times V\times H\times W\times C}$ coarsely. In Stage II, F_{SA} will be processed by a dual-branch parallel structure which contains EPMBs and EPTBs, to respectively generate refined and enhanced spatial-angular features $F_{SAM} \in \mathbb{R}^{U\times V\times H\times W\times C}$ and $F_{SAT} \in \mathbb{R}^{U\times V\times H\times W\times C}$. Subsequently, F_{Init}, F_{SAM}, and F_{SAT} are fused to generate the multi-level features $F_{Fuse} \in \mathbb{R}^{U\times V\times H\times W\times 3C}$:

$$F_{Fuse} = Conv(Concat(F_{Init}, F_{SAM}, F_{SAT})), \quad (5)$$

where $Conv(\cdot)$ denotes the convolution operation, and $Concat(\cdot)$ indicates concatenation along the channel dimension. Finally, F_{Fuse} undergoes an upsampling encoder $\mathcal{N}_{Rec}$, which consists of pixel shuffling layers and convolutional layers, to generate the final high-resolution image I_{HR}.

C. Subspace Simple Scanning and Subspace Simple Mamba Block

Inspired by [29], [32], we propose slicing 4D LF features into 2D subspaces, including the SAI pattern $F_s \in \mathbb{R}^{H\times W\times C}$ $(s = 1, \ldots, UV)$, the MacPI pattern $F_a \in \mathbb{R}^{U\times V\times C}$ $(a = 1, \ldots, HW)$, as well as the horizontal EPI pattern $F_{hor} \in \mathbb{R}^{V\times W\times C}$ $(hor = 1, \ldots, UH)$ and vertical EPI pattern $F_{ver} \in \mathbb{R}^{U\times H\times C}$ $(ver = 1, \ldots, VW)$. These features are then flattened through scanning. Furthermore, considering the coupling of LF subspace scanning, we design the Sub-SS strategy. Sub-SS has two core characteristics: (1) it replaces the traditional multi-directional scanning used in visual state space models with a unidirectional scanning approach to model feature correlations, and (2) it scans across

all subspaces to thoroughly capture the spatial-angular and geometric features of LF. As shown in Fig. 4(a), the Sub-SS strategy selects a specific pixel, referred to as the observation center (e.g., the blue pixel E). From this center, Sub-SS efficiently aggregates information from neighboring pixels in spatial domain and related pixels in angular domain, while also incorporating pixel disparity and geometric information from the epipolar plane. This process utiliz surrounding pixels (e.g., the blue pixel B, D, F, H and pixels of different colors E) to gather relevant spatial-angular information essential for accurately modeling feature distributions. The unidirectional scanning simplifies data aggregation, reducing computational complexity while enhancing the relevance of the information collected. Additionally, Sub-SS captures angular relationships by analyzing aligned pixels in angular domain and integrates geometric structure from the epipolar plane to improve the model's understanding of spatial relationships. In summary, Sub-SS combines unidirectional scanning with comprehensive subspace information to effectively model complex correlations in LF images, streamlining computation and improving performance in capturing spatial-angular and geometric features.

Building upon Sub-SS, we design the SSMB to efficiently extract features. Specifically, as shown in Fig. 4(b), different from the normal mamba structure, we replace causal convolutions with regular convolutions to eliminate the unidirectional limitation. Additionally, a symmetric branch, composed of an extra convolutional layer and SiLU activation, is introduced to compensate for potential information loss caused by the sequential modeling in Sub-SS. Subsequently, the outputs of two branches are concatenated and projected through a linear layer. This process effectively fuses sequential and spatial information, leveraging the complementary advantages of both features. Notably, to control the parameter size, the output of each branch is mapped to an embedding space with $C/2$ dimension. For the given input feature F_{in}, the output feature F_{out} of SSMB can be described as the following computation process:

$$\begin{aligned} F_1 &= SS\text{-}sub(\sigma(Conv(Linear(C, \frac{C}{2})(F_{in})))), \\ F_2 &= \sigma(Conv(Linear(C, \frac{C}{2})(F_{in}))), \\ F_{out} &= Linear(C, C)(Concat(F_1, F_2)), \end{aligned} \tag{6}$$

where F_1 and F_2 denote the intermediate features, σ denotes the sigmoid-weighted linear unit activation function, and $Linear(\cdot)$ denotes the linear mapping layer.

D. Dual-stage Non-local Spatial-Angular Correlations Modeling Strategy

The dual-stage modeling strategy can progressively model non-local spatial-angular correlations from coarse to fine. As shown in Fig. 3(b), similar to the approach in [57], we introduced a channel attention layer after SSMB to enhance interactions among channel features. Furthermore, a learnable residual mechanism was employed to construct RSMB. Specifically, for given features $F \in \mathbb{R}^{B\times H\times W\times C}$, the RSMB

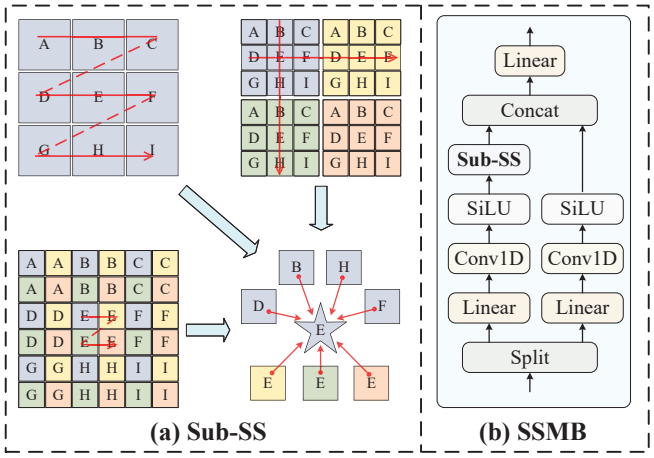

Fig. 4. (a) Sub-SS effectively models correlations between LF pixels and their nearest pixels in all subspaces through a simple unidirectional scanning. (b) The architecture of SSMB, which replaces causal convolution layers with regular convolution layers and introduces a symmetric path without SSM.

captures long-range dependency in pixels and outputs an optimized feature representation $\widehat{F} \in \mathbb{R}^{B\times H\times W\times C}$, formulated as follows:

$$\begin{aligned} \overline{F} &= SSMB(LN(F)) + s_1 \cdot F, \\ \widehat{F} &= CA(LN(\overline{F})) + s_2 \cdot \overline{F}, \end{aligned} \tag{7}$$

where $LN(\cdot)$ denotes layer normalization, $CA(\cdot)$ represents the channel attention layer, and s_1, s_2 are learnable residual connections.

1) Stage I – SA-RSMB for shallow spatial-angular feature coarse extraction in spatial and angular domains: Stage I, denoted as $H_{StageI}(\cdot)$, is primarily designed to integrate contextual information in spatial domain and complementary angular information in angular domain, mapping F_{Init} to F_{SA}. To achieve this, three cascaded SA-RSMBs and a local skip connection are used:

$$\begin{aligned} F_{SA} &= H_{StageI}(F_{Init}) + F_{Init}, \\ H_{StageI}(\cdot) &= SA\text{-}RSMB^3(SA\text{-}RSMB^2(SA\text{-}RSMB^1(\cdot))) \end{aligned} \tag{8}$$

where $SA\text{-}RSMB^i(\cdot), i \in [1, 2, 3]$ denotes i-th SA-RSMB.

The specific structure of SA-RSMB is shown in Fig. 3(c). We adopt a simple yet effective spatial-angular separable modeling method. First, the input feature $F \in \mathbb{R}^{U\times V\times H\times W\times C}$ is reshaped into $F_{SAI} \in \mathbb{R}^{UV\times H\times W\times C}$. It then passes through two RSMBs and a convolution for spatial domain feature interaction. This process integrates contextual information in spatial domain, generating the feature $F_S \in \mathbb{R}^{U\times V\times H\times W\times C}$ that contains fused spatial domain information:

$$F_S = Conv(RSMB^2(RSMB^1(F_{SAI}))) + F_{SAI}. \tag{9}$$

Next, F_S is reshaped into $F_{MacPI} \in \mathbb{R}^{HW\times U\times V\times C}$, and undergoes feature interaction in the angular domain via similar RSMBs and convolution. This process further utilizes complementary information in angular domain, generating the feature $F_{SA} \in \mathbb{R}^{U\times V\times H\times W\times C}$:

$$F_{SA} = Conv(RSMB^2(RSMB^1(F_{MacPI}))) + F_{MacPI}, \tag{10}$$

where $RSMB^j(\cdot), j \in [1, 2]$ denotes the j-th RSMB. The feature F_{SA} initially integrates spatial and angular domain

information, providing a foundation for feature refinement and enhancement in Stage II.

2) Stage II – EPMB and EPTB for deep refinement and enhancement of spatial-angular feature in epipolar plane domain: EPIs not only capture the spatial structure of edges or textures but also reflect disparity information through slanted lines with different slopes [32]. Therefore, Stage II further refines and enhances F_{SA} in epipolar plane domain, adaptively incorporating structure and disparity information into spatial-angular feature. To achieve this, we design a dual-branch parallel structure consisting of EPMB and EPTB to generate refined features $F_{SAM} \in \mathbb{R}^{U\times V\times H\times W\times C}$ and $F_{SAT} \in \mathbb{R}^{U\times V\times H\times W\times C}$:

$$\begin{aligned} F_{SAM} &= H_{StageII\text{-}M}(F_{SA}) \\ &= EPMB^3(EPMB^2(EPMB^1(F_{SA}))) + F_{SA}, \\ F_{SAT} &= H_{StageII\text{-}T}(F_{SA}) \\ &= EPTB^3(EPTB^2(EPTB^1(F_{SA}))) + F_{SA}, \end{aligned} \tag{11}$$

where $EPMB^m(\cdot), m \in [1,2,3]$ denotes the m-th EPMB, and $EPTB^n(\cdot), n \in [1,2,3]$ denotes the n-th EPTB.

EPMB is shown in Fig. 3(d), similar to the structure of SA-RSMB, we first reshape the feature F_{SA} from Stage I into horizontal EPI form $F_{EPI\_H} \in \mathbb{R}^{UH\times V\times W\times C}$ and vertical EPI form $F_{EPI\_V} \in \mathbb{R}^{VW\times U\times H\times C}$. Then, through RSMBs and convolutions, the disparity information in both horizontal and vertical directions interacts within epipolar plane domain. Notably, only two parameter-shared RSMBs and two convolutions are used in EPMB, which further optimizes computational resources:

$$\begin{aligned} F_{EPI\_V} &= Conv(RSMB(F_{EPI\_H})) + F_{EPI\_H}, \\ F_{SAM} &= Conv(RSMB(F_{EPI\_V})) + F_{EPI\_V}. \end{aligned} \tag{12}$$

The EPMB is capable of capturing disparity and structural feature in epipolar plane domain. However, compressing these features into limited hidden states may lead to insufficient refinement and enhancement of spatial-angular feature. Therefore, we introduce the Transformer-based EPTB. It has two advantages: (1) compared to feature interaction in spatial or angular domains, the sequence formed by pixel unfolding in epipolar plane domain is relatively short, thus not significantly increasing the computational complexity; (2) experiments show that features extracted by EPTB and EPMB are complementary to each other. The joint use of both can fully leverage their respective advantages, enhancing the richness of feature representations. The structure of EPTB is shown in Fig. 3(e). In this block, we replace the RSMBs in EPMB with Simple Transformer Block (STB):

$$\begin{aligned} F_{EPI\_V} &= Conv(STB(F_{EPI\_H})) + F_{EPI\_H}, \\ F_{SAM} &= Conv(STB(F_{EPI\_V})) + F_{EPI\_V}. \end{aligned} \tag{13}$$

Specifically, taking feature $F_{EPI\_H} \in \mathbb{R}^{UH\times V\times W\times C}$ as an example, we first reshape F_{EPI_H} into an embedding sequence $x \in \mathbb{R}^{UH\times VW\times C}$, which serves as the input to STB. Q, K, V are generated through three linear projection layers $W_Q, W_K, W_V \in \mathbb{R}^{C\times C}$:

$$Q = xW_Q, \quad K = xW_K, \quad V = xW_V, \tag{14}$$

where Q, K, V represent the query, key, and value matrices.

Similar to [60], Self-Attention (SA) is performed in P independent subspaces to compute Multi-head Self-Attention (MSA):

$$SA_p(Q_p, K_p, V_p) = \text{softmax}\left(\frac{Q_p(K_p)^T}{\sqrt{C/P}}\right)V_p, \tag{15}$$

where $p = 1, 2, \ldots, P$. The results from all self-attention heads are concatenated along the channel dimension and projected to produce the weighted sequence $\overline{x} \in \mathbb{R}^{UH\times VW\times C}$:

$$\overline{x} = Concat(SA_1, SA_2, \ldots, SA_P)W_P + x, \tag{16}$$

where $W_P \in \mathbb{R}^{C\times C}$ is the linear projection matrix.

Furthermore, we adopt a feed-forward network layer to introduce local attributes and pixel position awareness, enhancing the spatial information perception capability of STB:

$$\widehat{x} = MLP(DWConv(LN(\overline{x}))) + \overline{x}, \tag{17}$$

where $DWConv(\cdot)$ is the depth-wise convolution, and $\widehat{x} \in \mathbb{R}^{UH\times V\times W\times C}$ is the final output sequence, which adaptively incorporates the horizontal disparity structure. Next, the same processing steps are applied to $F_{EPI\_V} \in \mathbb{R}^{VW\times U\times H\times C}$, incorporating the vertical disparity structure.

IV. Experiments

A. Experiment Settings

1) Datasets: To ensure fairness and comparability, we use five widely adopted LFSR benchmark datasets: EPFL [61], HCIold [62], HCInew [63], INRIA [64], and STFgantry [65], based on settings from previous works [18], [31], [40]. These datasets contain 144 training scenes and 23 test scenes, covering diverse content and disparity distributions. We extract 5×5 center view images to crop them into high-resolution patches (32×32 and 64×64), and generate corresponding low-resolution patches (16×16) using bicubic interpolation for $\times 2$ and $\times 4$ LFSR tasks.

2) Implementation Details: All experiments are conducted on a single NVIDIA RTX A6000 GPU using the PyTorch framework. The LFMT network is trained with $L1$ loss and optimized using Adam with $\beta_1 = 0.9$ and $\beta_2 = 0.999$. The batch size is 2, with an initial learning rate of 2×10^{-4}, halved every 15 epochs. Training runs for 90 epochs.

3) Baseline Methods and Metrics: We compare our method with several state-of-the-art SR methods, including three single-image methods: Bicubic interpolation, EDSR [58], and RCAN [59]; seven CNN-based LFSR methods: resLF [13], LFSSR [14], LF-InterNet [39], LF-ATO [15], LF-IINet [20], DistgSSR [40], and HLFSR [28]; four Transformer-based methods: LFT [29], DPT [30], EPIT [32], and LF-DET [31]; and one Mamba-based method: MLFSR [34]. To evaluate image quality, we use two widely adopted metrics: Peak Signal-to-Noise Ratio (PSNR) and Structural Similarity Index (SSIM).

TABLE I
QUANTITATIVE COMPARISON (PSNR/SSIM) OF DIFFERENT METHODS FOR × 2 AND × 4 LFSR. THE BEST AND SECOND-BEST RESULTS ARE MARKED IN RED AND BLUE. THE PARAMS. AND FLOPS ARE CALCULATED ON AN INPUT LF IMAGE WITH SIZE 5 × 5 × 32 × 32

Method	Scale	Params.(M)	FLOPs(G)	EPFL	HCInew	HCIold	INRIA	STFgantry	Average
				PSNR/SSIM	PSNR/SSIM	PSNR/SSIM	PSNR/SSIM	PSNR/SSIM	PSNR/SSIM
Bicubic	× 2	-	-	29.50/0.9350	31.69/0.9335	37.46/0.9776	31.10/0.9563	30.82/0.9473	31.11/0.9542
EDSR [58]	× 2	38.62	989	33.09/0.9631	34.83/0.9594	41.01/0.9875	34.97/0.9765	36.29/0.9819	36.04/0.9737
RCAN [59]	× 2	15.31	389.75	33.16/0.9635	34.98/00.9602	41.05/0.9875	35.01/0.9769	36.33/0.9825	36.11/0.9742
resLF [13]	× 2	7.98	37.06	32.75/0.9672	36.07/0.9715	42.61/0.9922	34.57/0.9784	36.89/0.9873	36.58/0.9793
LFSSR [14]	× 2	0.88	25.70	33.69/0.9748	36.86/0.9753	43.75/0.9939	35.27/0.9834	38.07/0.9902	37.73/0.9835
LF-InterNet [39]	× 2	5.04	47.46	34.14/0.9761	37.28/0.9769	44.45/0.9945	35.80/0.9846	38.72/0.9916	38.08/0.9847
LF-ATO [15]	× 2	1.22	597.66	34.27/0.9757	37.24/0.9767	44.20/0.9942	36.15/0.9842	39.64/0.9929	38.15/0.9843
LF-IINet [20]	× 2	4.84	56.16	34.68/0.9773	37.74/0.9790	44.84/0.9948	36.57/0.9853	39.86/0.9936	38.74/0.9857
DistgSSR [40]	× 2	3.53	64.11	34.81/0.9787	37.96/0.9796	44.94/0.9949	36.59/0.9859	40.40/0.9942	38.94/0.9866
HLFSR [28]	× 2	13.72	167.40	35.31/0.9800	38.32/0.9807	44.98/0.9950	37.06/0.9867	40.85/0.9947	39.30/0.9874
LFT [29]	× 2	1.11	56.16	34.80/0.9781	37.84/0.9791	44.52/0.9945	36.59/00.9855	40.51/0.9941	38.85/0.9863
DPT [30]	× 2	3.73	65.34	34.48/0.9758	37.35/0.9771	44.31/0.9943	36.40/0.9843	39.52/0.9926	38.40/0.9848
EPIT [32]	× 2	1.42	69.71	34.83/0.9775	38.23/0.9810	45.08/0.9949	36.67/0.9853	42.17/0.9957	39.40/0.9877
LF-DET [31]	× 2	1.59	48.50	35.26/0.9797	38.31/0.9807	44.99/0.9950	36.95/0.9864	41.76/0.9955	39.45/0.9875
MLFSR [34]	× 2	1.36	-	35.22/0.9801	38.14/0.9803	44.90/0.9950	36.92/0.9865	40.98/0.9949	39.23/0.9874
LFMT	× 2	2.06	63.18	35.52/0.9812	38.46/0.9815	45.03/0.9950	37.21/0.9871	41.92/0.9956	39.63/0.9881
LFMT*	× 2	2.06	63.18	35.65/0.9819	38.67/0.9821	45.31/0.9952	37.30/0.9875	42.30/0.9959	39.85/0.9885
Bicubic	× 4	-	-	25.26/0.8324	27.72/0.8517	32.58/0.9344	26.95/0.8867	26.09/0.8452	27.72/0.8701
EDSR [58]	× 4	38.89	1017	27.84/0.8854	29.60/0.8869	35.18/0.9536	29.66/0.9257	28.70/0.9072	30.20/0.9118
RCAN [59]	× 4	15.36	408.5	27.88/0.8863	29.63/0.8886	35.20/0.9548	29.76/0.9276	28.90/0.9131	30.27/0.9141
resLF [13]	× 4	8.64	39.70	28.27/0.9035	30.73/0.9107	36.71/0.9682	30.34/0.9412	30.19/0.9372	31.25/0.9322
LFSSR [14]	× 4	1.77	128.44	28.27/0.9118	30.72/0.9145	36.70/0.9696	30.31/0.9467	30.15/0.9426	31.52/0.9370
LF-InterNet [39]	× 4	5.48	50.10	28.67/0.9162	30.98/0.9161	37.11/0.9716	30.64/0.9491	30.53/0.9409	31.58/0.9388
LF-ATO [15]	× 4	1.36	686.99	28.52/0.9115	30.88/0.9135	37.00/0.9699	30.71/0.9484	30.61/0.9430	31.54/0.9373
LF-IINet [20]	× 4	4.88	57.42	29.11/0.9188	31.36/0.9208	37.62/0.9734	31.08/0.9515	31.21/0.9502	32.08/0.9429
DistgSSR [40]	× 4	3.58	65.41	28.99/0.9195	31.38/0.9217	37.56/0.9732	30.99/0.9519	31.65/0.9535	32.11/0.9440
HLFSR [28]	× 4	13.87	182.52	29.20/0.9222	31.57/0.9238	37.78/0.9742	31.24/0.9534	31.64/0.9537	32.29/0.9455
LFT [29]	× 4	1.16	57.60	29.25/0.9210	31.46/0.9218	37.63/0.9735	31.20/0.9524	31.86/0.9548	32.28/0.9447
DPT [30]	× 4	3.78	66.55	28.93/0.9170	31.19/0.9188	37.39/0.9721	30.96/0.9503	31.14/0.9488	31.93/0.9414
EPIT [32]	× 4	1.47	74.96	29.34/0.9197	31.51/0.9231	37.68/0.9737	31.37/0.9526	32.18/0.9571	32.40/0.9452
LF-DET [31]	× 4	1.69	51.20	29.47/0.9230	31.56/0.9235	37.84/0.9744	31.39/0.9534	32.14/0.9573	32.48/0.9463
MLFSR [34]	× 4	1.41	-	29.28/0.9218	31.56/0.9235	37.83/0.9745	31.24/0.9531	32.03/0.9567	32.39/0.9459
LFMT	× 4	2.19	66.72	29.74/0.9239	31.69/0.9251	37.83/0.9744	31.82/0.9544	32.23/0.9577	32.66/0.9471
LFMT*	× 4	2.19	66.72	29.83/0.9255	31.86/0.9268	38.01/0.9750	31.89/0.9553	32.50/0.9595	32.82/0.9484

Notes: * denotes geometry assembling strategy.

B. Comparison to State-of-the-Arts

1) Quantitative Results: Table I presents the quantitative comparison results of LFMT with several advanced methods. On both × 2 and × 4 LFSR tasks, our method demonstrates superior performance, significantly outperforming CNN-based and Transformer-based methods, while maintaining a moderate model complexity. Specifically, for × 2 LFSR, our method achieves the highest average PSNR and SSIM, with a 0.18 dB improvement in average PSNR over the second-best method LF-DET, showcasing excellent reconstruction capability. For the more challenging × 4 LFSR, our method also shows significant improvements in PSNR and SSIM, with a 0.18 dB and 0.008 increase over LF-DET, respectively. Notably, on real-world datasets such as EPFL and INRIA, our method perform well in modeling complex LF structures and image details, further validating its robustness and broad applicability in real-world scenarios.

In-depth performance analysis shows that our method exhibits clear advantages on datasets with large disparities, highlighting its exceptional ability to model long-range correlations in LF images. For example, for the × 4 LFSR, on the STFgantry dataset, our method improves 0.05 dB in PSNR over the EPIT which excels in large disparity scenes. Meanwhile, the strong performance of our method on mid-to-small disparity datasets, such as the HCInew dataset, highlights its strong compatibility and adaptability in local feature extraction. It is worth noting that on the HCIold dataset, our method slightly lags behind LF-DET, which excels in small disparity and smooth regions due to its multi-scale angular modeling. However, our approach leverages comprehensive spatial, angular, and epipolar interaction to build non-local angular correlations from coarse to fine levels. This holistic modeling improves feature interaction efficiency across subspaces and excels in handling large disparities, complex structures, and artifact reduction. Furthermore, we employed a geometric assembly strategy to further improve overall performance.

2) Qualitative Results: As shown in Fig. 5, for × 2 SR our method effectively restores image details, particularly excelling in texture recovery. For instance, in the *Red_ & White_Building* scene, our method successfully pre-

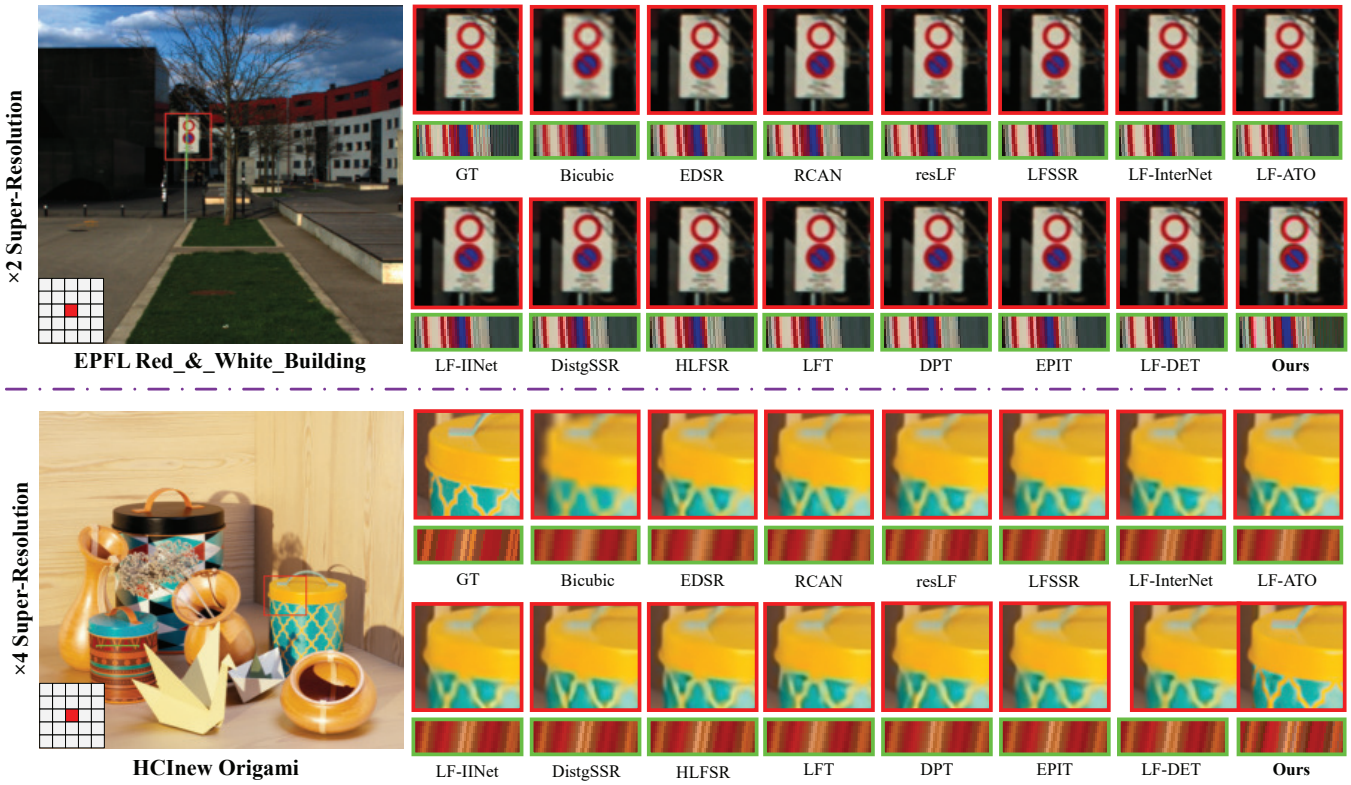

Fig. 5. Comparison of visual results for the × 2 and × 4 SR with state-of-the-art methods. As shown in the figure, the enlarged spatial patches of the center SAIs are highlighted with red boxes, and the enlarged EPI slices are highlighted with green boxes.

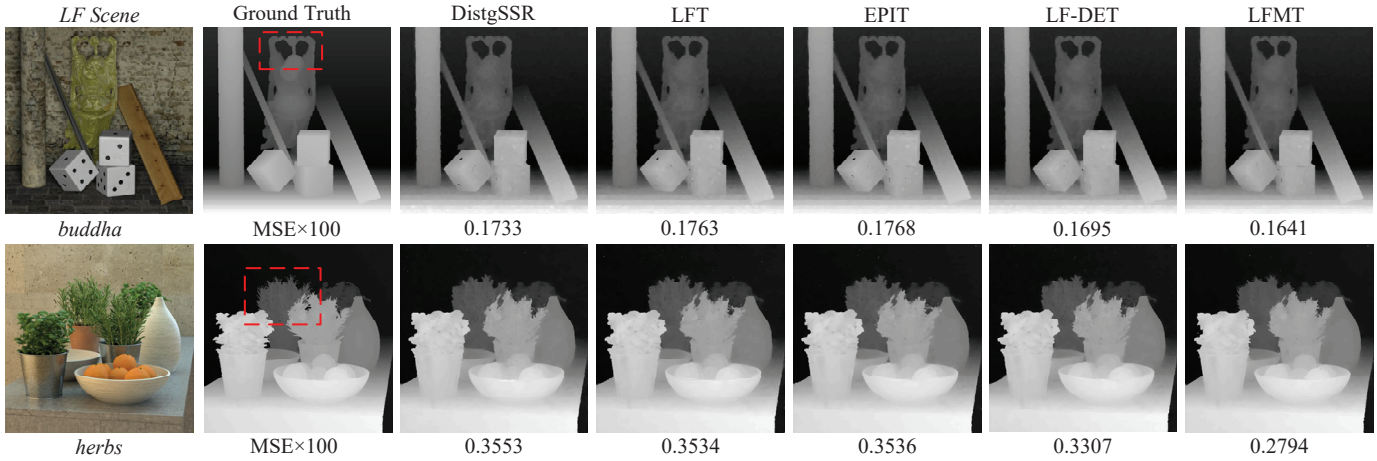

Fig. 6. Depth estimation results achieved by SPO [66] using × 4 SR LF images generated by different LFSR methods. The mean square error multiplied by 100 ($MSE \times 100$) is chosen as the quantitative metric.

serves the fine texture of the parking sign and recovers more details in the vertical EPI region. Moreover, our method demonstrates significant advantages in utilizing LF angular information, effectively modeling the spatial-angular correlations, especially in scenes with repetitive textures. For the more challenging × 4 SR, our method demonstrates a significant advantage in detail recovery and edge sharpening. For example, in the *Origami* scene, our method precisely recovers the edges of the crossed lines on the surface of can, outperforming other methods in avoiding common blurring and artifacts, demonstrating excellent detail restoration capability. Due to LFMT, which can integrate multi-level information from spatial, angular, and epipolar plane domains, it shows unique advantages in modeling long-range and fine-grained angular relationships, as demonstrated in the recovery of the horizontal EPI region in *Origami* scene.

3) Angular Consistency: We conduct analysis from two aspects to evaluate the angular consistency of LFMT. First, we visualize the horizontal or vertical EPI slices from different scenes, as shown in Fig. 5. The EPI slices processed by our method exhibit smoother slanted line textures, outperforming the results of other LFSR methods. For instance, in the *Origami* scene, the EPI slices generated by LFMT have clearer textures and effectively avoid artifacts, demonstrating higher angular consistency. Second, we perform depth estimation using the SPO algorithm proposed in [66], selecting the *Buddha* and *Herbs* scenes as test objectives. As shown in Fig. 6, the depth maps generated by LFMT have sharper edge

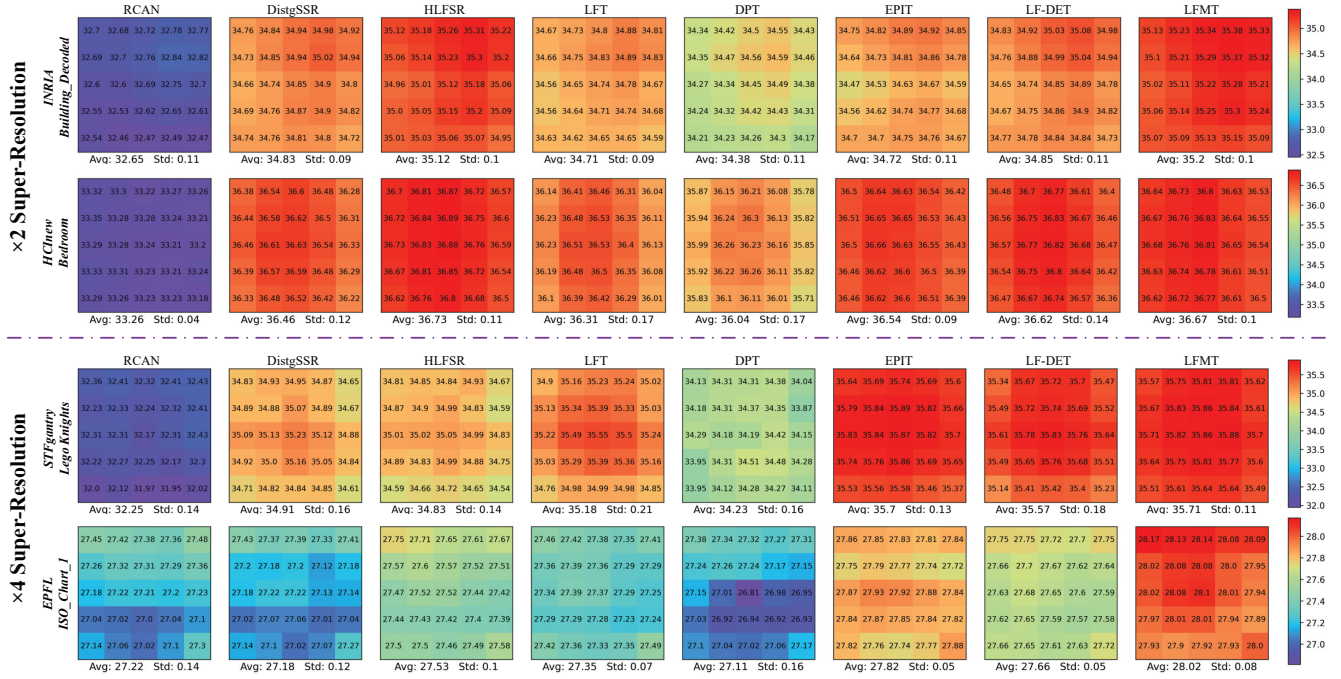

Fig. 7. Comparison in terms of PSNR distribution among different views for × 2 and × 4 SR. Average PSNR and standard deviation for each scene are also listed.

TABLE II
COMPARISON OF PARAMETERS AND FLOPS BETWEEN LFMT AND COMPETING METHODS ON × 4 SUPER-RESOLUTION

Method	Scale	Params.(M)	FLOPs(G)	PSNR
DistgSSR	× 4	3.58	65.41	32.11
HLFSR	× 4	13.87	182.52	32.29
LFT	× 4	1.16	57.60	32.28
DPT	× 4	3.78	66.55	31.93
EPIT	× 4	1.47	74.96	32.40
LF-DET	× 4	1.69	51.20	32.48
LFMT (tiny)	× 4	1.37	42.33	32.48
LFMT	× **4**	**2.19**	**66.72**	**32.66**

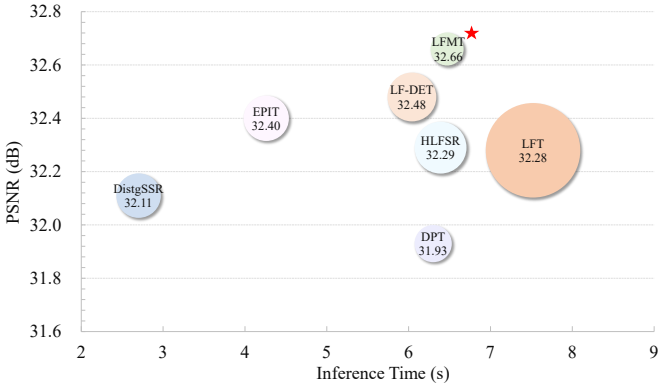

Fig. 8. Computational efficiency comparison between LFMT and state-of-the-art methods on × 4 SR. The area of circles denotes memory consumption. The inference time is calculated by averaging inference time of all scenes across the five test datasets.

textures and lower angular deviation. Our method achieves the best scores in both scenes, further proving its superior angular consistency.

TABLE III
ABLATION RESULTS (PSNR/SSIM) COMPARISON OF SUB-SS AND OTHER SCANNING STRATEGIES FOR × 4 SUPER-RESOLUTION

Scanning strategy	Params.(M)	Ave.PSNR/SSIM
Sub-SS	**2.19**	**32.66/0.9471**
SS2D	2.26	32.52/0.9468
Cross-SS2D	2.26	32.55/0.9470
SS4D	2.34	32.52/0.9471

4) Performance w.r.t. Perspectives: We further evaluate the reconstruction performance of different methods across different views in the same scene, validating the advantage of LFMT in leveraging non-local spatial-angular information to enhance SR quality. In both × 2 and × 4 SR tasks, we select several representative scenes with a 5 × 5 angular resolution. The PSNR values and standard deviations for each view image are calculated and compared with various advanced methods. As shown in Fig. 7, our method significantly reduces the standard deviation while achieving the highest PSNR values in most scenes. This performance improvement is attributed to the dual-stage non-local spatial-angular correlations modeling strategy, which performs feature extraction in all subspaces. This strategy effectively facilitates the interaction of non-local spatial-angular features in different views, enhancing angular consistency and enabling balanced optimization of LFSR performance for each view.

5) Computational Efficiency: To evaluate the computational efficiency of LFMT, we compare its inference time and GPU memory usage with several competitive models, as shown in Fig. 8. In general, compared to CNN-based methods, the inference time of LFMT is slightly increased, while it shows a more competitive inference speed than Transformer-based methods. Notably, LFMT requires less memory consumption

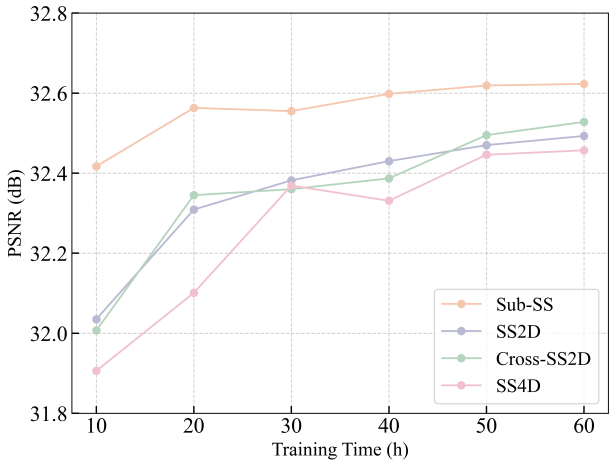

Fig. 9. Comparison of PSNR vs. Training Time between Sub-SS and three other scanning strategies with similar parameters on × 4 SR.

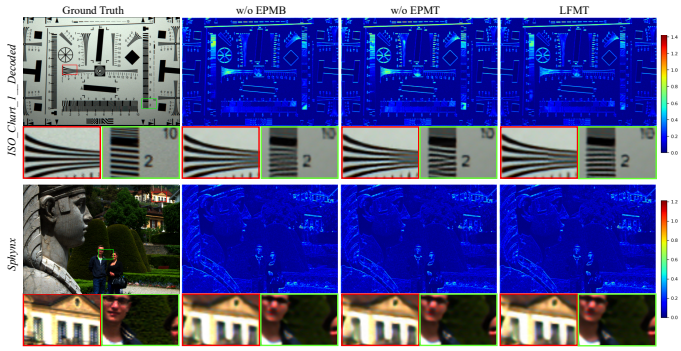

Fig. 10. Visual results of the reconstructed central view images achieved by different enhancement branches. We also present the error map between the results and ground truth.

while achieving a significant improvement in PSNR. On the other hand, in Table II, we compare the parameters and FLOPs of LFMT with other competing methods. Specifically, we reduced the network depth and trained a tiny LFMT model. Benefiting from the Sub-SS strategy, which reduces redundant computations in subspaces, the tiny LFMT model efficiently simplifies the feature modeling process of LF images. As a result, it achieves the highest PSNR performance with the lowest parameters and FLOPs. Overall, our method strikes a better balance between computational complexity and reconstruction performance, enabling LFMT to efficiently perform LFSR task in resource-constrained hardware environments.

6) Limitation: In the × 2 SR, our method does not achieve the highest PSNR on the HCIold [62] and STFgantry [65] datasets. In particular, on STFgantry [65], it is about 0.25 dB lower than EPIT [32], likely due to large-disparity structures and locally complex textures, which create a trade-off between local detail recovery and fine-grained angular correlation modeling. Moreover, although LFMT is more computationally efficient than pure Transformer methods, its deployment on resource-constrained devices remains challenging, indicating the need for further model compression and inference optimization.

TABLE IV
ABLATION RESULTS (PSNR/SSIM) ON THE EFFECTIVENESS OF SA-RSMB, EPMB, EPTB COMPONENTS FOR × 2 AND × 4 SUPER-RESOLUTION

The framework	Scale	Params.(M)	FLOPs(G)	Ave.PSNR/SSIM
LFMT w/o SA-RSMB	× 2	2.10	84.66	39.52/0.9878
LFMT w/o EPMB	× 2	2.41	64.09	39.56/0.9880
LFMT w/o EPTB	× 2	2.37	71.16	39.12/0.9875
LFMT (ours)	× **2**	**2.04**	**62.76**	**39.63/0.9881**
LFMT w/o SA-RSMB	× 4	2.32	86.72	32.56/0.9467
LFMT w/o EPMB	× 4	2.56	68.04	32.60/0.9470
LFMT w/o EPTB	× 4	2.15	73.79	32.46/0.9467
LFMT (ours)	× **4**	**2.19**	**66.72**	**32.66/0.9471**

TABLE V
ABLATION RESULTS (PSNR/SSIM) ON THE DUAL-STAGE NON-LOCAL SPATIAL-ANGULAR CORRELATIONS MODELING STRATEGY AND STRUCTURAL VARIANTS FOR × 4 SUPER-RESOLUTION

Stage I	Stage II	Params.	Ave.PSNR/SSIM
SA-RSMB	**EPTB+EPMB/Parallel**	**2.19**	**32.66/0.9471**
EPTB+EPMB /Parallel	SA-RSMB	2.19	32.44/0.9462
SA-RSMB	EPMB+EPTB/Sequential	2.19	32.59/0.9470
SA-RSMB	EPTB+EPMB/Sequential	2.19	32.63/0.9471

C. Ablation experiments

In this section, we conduct a series of ablation experiments to investigate the contributions of different components in LFMT network. The experiments include validating the effectiveness of the Sub-SS strategy, SA-RSMB, EPMB, and EPTB components, as well as analyzing the performance of the LFMT network architecture, its hybrid design compared with pure Mamba and pure Transformer models, and its variants. Additionally, we examine the impact of the number of components on model performance and verify the role of hierarchical feature fusion in enhancing LFSR performance. For clarity, the bold entries in the table denote the baseline configuration employed by LFMT.

1) The SS-Sub Strategy: The Sub-SS strategy aims to address the coupling issue present in multi-directional scanning in LF subspaces, thereby improving feature extraction efficiency. To validate the effectiveness of Sub-SS in enhancing computational efficiency while maintaining high performance, we compare it with bidirectional scanning (SS2D [36]), cross-bidirectional scanning (Cross-SS2D) and four-way scanning (SS4D [37]). As shown in Table III, for the × 4 SR task, the PSNR values significantly decrease with multi-directional scanning under similar parameter settings. This is because multi-directional scanning leads to redundant modeling of features, causing noise and redundant features to be overly amplified in subspaces, which weakens the recovery of high-frequency details. Further comparisons reveal the advantages of the Sub-SS strategy in training time and model performance. Fig. 9 shows the change in the PSNR indicator over time compared with the other three scanning strategies. We observe that under comparable parameter settings, the Sub-SS strategy rapidly converges to a high PSNR value, significantly reducing training time.

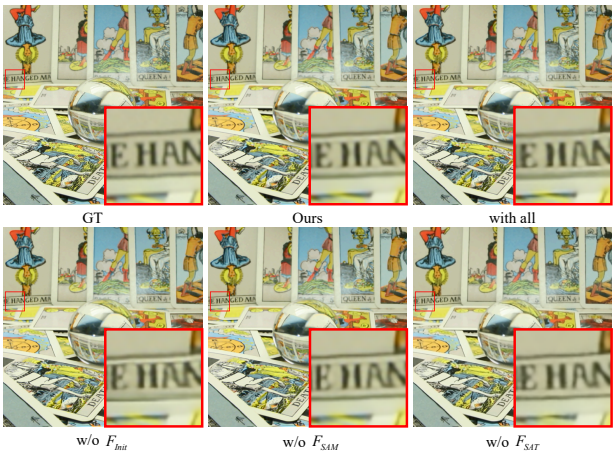

Fig. 11. Visualization of the impact of missing features at different levels on the results of × 4 SR.

TABLE VI
ABLATION RESULTS (PSNR/SSIM) OF PURE MAMBA, PURE TRANSFORMER, AND LFMT FOR × 4 SUPER-RESOLUTION

The framework	Params.(M)	FLOPs(G)	Ave.PSNR/SSIM
Pure Mamba	2.16	74.89	32.51/0.9468
Pure Transformer	2.23	78.62	32.54/0.9469
LFMT	**2.19**	**66.72**	**32.66/0.9471**

2) Effectiveness of SA-RSMB, EPMB, and EPTB Components: We evaluate the contributions of the SA-RSMB, EPMB, and EPTB components in the LFMT network by removing each component and retraining the network. To ensure a fair comparison, we adjust the network depth to maintain similar parameters. As shown in Table IV, removing any of these components leads to a significant decrease in PSNR values for both × 2 and × 4 LFSR tasks. This is because SA-RSMB effectively selects and interacts with important features in both spatial and angular domains, while the EPMB and EPTB process and enhance deep spatial-angular features in epipolar plane domain, strengthening spatial-angular correlations. Fig. 10 presents visual comparisons showing the impact of missing EPMB or EPTB components, further confirming the synergistic effect of EPMB and EPTB. These components are crucial for feature extraction and interaction in all subspaces of LF images, significantly contributing to the improvement of LFSR performance.

3) Dual-stage Non-local Spatial-angular Correlations Modeling Strategy and Structural Variants: We conduct an in-depth ablation study on the structure and variants of the dual-stage non-local spatial-angular correlation modeling in LFMT. As shown in Table V, we first examine the impact of swapping the order of feature extraction in spatial-angular domain and epipolar plane domain. In the baseline LFMT, Stage I employs SA-RSMB for coarse spatial-angular feature extraction, followed by Stage II with EPTB and EPMB for fine epipolar feature enhancement, achieving a PSNR of 32.66 dB. In contrast, the "reversed stage order" experiment first extracts epipolar features with EPTB and EPMB, and then applies SA-RSMB in Stage II for spatial-angular feature extraction, which results in a lower PSNR of 32.44 dB

TABLE VII
ABLATION RESULTS (PSNR/SSIM) ON THE NUMBER OF SA-RSMB, EPMB, EPTB COMPONENTS FOR × 4 SUPER-RESOLUTION

Number of SA-RSMB	Number of EPIM/EPIT	Params.(M)	FLOPs(G)	Ave.PSNR/SSIM
3	**3**	**2.19**	**66.72**	**32.66/0.9471**
1	3	1.51	50.11	32.46/0.9454
2	3	1.85	58.41	32.61/0.9467
4	3	2.53	75.02	32.64/0.9470
3	1	1.61	44.26	32.35/0.9454
3	2	1.90	55.49	32.53/0.9465
3	4	2.48	77.95	32.63/0.9470

TABLE VIII
ABLATION RESULTS (PSNR/SSIM) ON THE HIERARCHICAL FEATURE FUSION FOR × 4 SUPER-RESOLUTION

The framework	Params.(M)	FLOPs(G)	Ave.PSNR/SSIM
with all	2.25	68.39	32.62/0.9471
w/o F_{Init}	2.19	66.72	32.60/0.9469
w/o F_{SA}	**2.19**	**66.72**	**32.66/0.9471**
w/o F_{SAT}	2.19	66.72	32.37/0.9457
w/o F_{SAM}	2.19	66.72	32.58/0.9467

(a drop of 0.22 dB). This comparison demonstrates that performing coarse spatial-angular extraction first, followed by epipolar refinement, is both reasonable and essential. Such a design sequence is more favorable for effectively modeling non-local spatial-angular correlations in LF images. This is because, at deeper network layers, the intertwined spatial-angular information in epipolar plane domain more accurately represents disparity information and inherent structures, thereby facilitating high-quality recovery and modeling of non-local spatial-angular features. Additionally, we compare the performance of sequential and parallel configurations of the EPMB and EPTB components. The results indicate that the parallel configuration better leverages the potential of these components in the spatial-angular feature refinement stage. This configuration promotes the complementary advantages of EPMB and EPTB, effectively enhancing the LFSR performance.

4) Comparison of Pure Mamba, Pure Transformer, and LFMT: To further validate the complementarity between the Mamba and Transformer mechanisms, we conducted a structural-level comparison among three full model variants: a pure Mamba network, a pure Transformer network, and the proposed hybrid LFMT network. As shown in Table VI, the hybrid LFMT network achieves the best overall performance, with PSNR improvements of 0.15 dB over the pure Mamba network and 0.12 dB over the pure Transformer network, significantly outperforming the two single-mechanism networks. We attribute this performance gain to the hybrid design of LFMT, which integrates both state space modeling and self-attention modeling paradigms. This integration effectively enlarges the receptive field and allows more comprehensive modeling of non-local spatial-angular correlations across multiple subspaces in the LF data. By combining the efficient long-range dependency modeling capability of Mamba with the fine-grained feature representation of Transformer, LFMT

demonstrates superior reconstruction quality and enhanced generalization. These results fully validate the advantage of the hybrid paradigm in LF modeling.

5) Number of SA-RSMB, EPMB, EPTB Components: In Table VII, we provide a detailed analysis of the impact of different quantities of SA-RSMB and EPMB/EPTB on the overall performance of LFMT. Notably, the counts of EPMB and EPTB components remain identical. The bolded data in the first row represents the configuration adopted by our method, where the number of SA-RSMB, EPMB and EPTB is set to 3. The experimental results show that, when the number of EPMB/EPTB is fixed at 3, as the number of SA-RSMB increases from 1 to 4, the Ave.PSNR/SSIM first increases and then decreases, reaching its peak when the number of SA-RSMB is 3. Similarly, when the number of SA-RSMB is fixed at 3, as the number of EPMB/EPTB increases from 1 to 4, the Ave.PSNR/SSIM also follows a trend of first increasing and then decreasing, stabilizing when the number of EPMB/EPTB is 3. These results clearly indicate that the number of SA-RSMB and EPMB/EPTB components significantly affects the performance of LFMT. Too few components may result in inadequate feature learning, while too many can lead to overfitting. After considering both model complexity and network performance, we determined that the optimal configuration is to set the number of SA-RSMB, EPMB and EPTB to 3. This configuration ensures efficient operation of the LFMT network while achieving the best LFSR performance.

6) Hierarchical Feature Fusion: We conduct ablation experiments on feature fusion at different layers to investigate the impact of hierarchical feature fusion on model performance. Specifically, we respectively remove F_{Init}, F_{SA}, F_{SAT}, F_{SAM}, and conduct performance evaluations for the ×4 LFSR task. As shown in Table VIII, we are surprised to find that the fusion of only F_{Init}, F_{SAT}, and F_{SAM} can maximally unleash the potential of LFMT, achieving the highest performance. In particular, removing F_{Init} only slightly affects the performance, while adding F_{SA} leads to a decline in performance. Furthermore, the removal of F_{SAT} or F_{SAM} disrupts the interaction of deep features within the epipolar plane domain, thereby weakening the model's capacity to leverage disparity information and accurately model the intrinsic LF structure. This has a significant detrimental impact on overall performance. Fig. 11 visualizes the effects of missing features at various levels on the results. These experimental results demonstrate that hierarchical feature fusion plays a crucial role in the LFSR task. And it is essential to ensure that the LFSR network effectively captures and integrates feature information across multiple levels, including spatial, angular, and epipolar plane domains.

V. Conclusion

SSMs have shown promise in visual tasks, but faces challenges in LFSR due to the dense and complex 4D correlations far exceeding those in 2D images. This paper introduces LFMT, a LFSR network that leverages non-local spatial-angular information in complete LF subspaces to showcase the potential of SSMs in LFSR tasks. By incorporating the Sub-SS strategy and optimizing the Mamba structure, LFMT enhances long-range dependency modeling and computational efficiency. Additionally, we propose a dual-stage modeling strategy for deep non-local spatial-angular correlations modeling and combine the feature extraction strengths of SSM and Transformer models to comprehensively explore disparity information and LF intrinsic structure information. Comparative experiments demonstrate that LFMT achieves superior performance over CNN-based and Transformer-based methods, highlighting its ability to utilize complete subspace information effectively. LFMT's interactive modeling of spatial-angular-epipolar subspaces offers a transferable framework for various LF processing tasks. In future work, we will explore extending LFMT to other LF reconstruction and enhancement applications, such as angular super-resolution.

References

[1] G. Wu *et al.*, "Light field image processing: An overview," *IEEE J. Sel. Topics Signal Process*, vol. 11, no. 7, pp. 926–954, Oct. 2017.

[2] Y. Wang, J. Yang, Y. Guo, C. Xiao, and W. An, "Selective light field refocusing for camera arrays using bokeh rendering and superresolution," *IEEE Signal Process. Lett.*, vol. 26, no. 1, pp. 204–208, Jan. 2019.

[3] S. S. Jayaweera, C. U. Edussooriya, C. Wijenayake, P. Agathoklis, and L. T. Bruton, "Multi-volumetric refocusing of light fields," *IEEE Signal Process. Lett.*, vol. 28, pp. 31–35, Dec. 2020.

[4] H.-G. Jeon, J. Park, G. Choe, J. Park, Y. Bok, Y.-W. Tai, and I. S. Kweon, "Depth from a light field image with learning-based matching costs," *IEEE Trans. Pattern Anal. Mach. Intell.*, vol. 41, no. 2, pp. 297–310, Feb. 2019.

[5] Y. Zhang, W. Dai, M. Xu, J. Zou, X. Zhang, and H. Xiong, "Depth estimation from light field using graph-based structure-aware analysis," *IEEE Trans. Circuits Syst. Video Technol.*, vol. 30, no. 11, pp. 4269–4283, Nov. 2020.

[6] J. Chen, J. Hou, Y. Ni, and L.-P. Chau, "Accurate light field depth estimation with superpixel regularization over partially occluded regions," *IEEE Trans. Image Process.*, vol. 27, no. 10, pp. 4889–4900, 2018.

[7] J. Jin and J. Hou, "Occlusion-aware unsupervised learning of depth from 4-d light fields," *IEEE Trans. Image Process.*, vol. 31, pp. 2216–2228, 2022.

[8] P. Zhou, L. Shi, X. Liu, J. Jin, Y. Zhang, and J. Hou, "Light field depth estimation via stitched epipolar plane images," *IEEE Trans. Vis. Comput. Graph.*, vol. 30, no. 10, pp. 6866–6879, 2023.

[9] J. Zhang, Y. Yao, and L. Quan, "Learning signed distance field for multi-view surface reconstruction." in *Proc. IEEE Int. Conf. Comput. Vis. (ICCV)*, 2021, pp. 6505–6514.

[10] J. Yu, "A light-field journey to virtual reality," *IEEE MultiMedia*, vol. 24, no. 2, pp. 104–112, Apr. 2017.

[11] S. Choi, M. Gopakumar, Y. Peng, J. Kim, and G. Wetzstein, "Neural 3d holography: Learning accurate wave propagation models for 3d holographic virtual and augmented reality displays," *ACM Trans. Graph.*, vol. 40, no. 6, pp. 1–12, 2021.

[12] Y. Yoon, H.-G. Jeon, D. Yoo, J.-Y. Lee, and I. So Kweon, "Learning a deep convolutional network for light-field image super-resolution," in *Proc. IEEE Int. Conf. Comput. Vis. Workshops*, 2015, pp. 24–32.

[13] S. Zhang, Y. Lin, and H. Sheng, "Residual networks for light field image super-resolution," in *Proc. IEEE Conf. Comput. Vis. Pattern Recognit. (CVPR)*, Jun. 2019, pp. 11 046–11 055.

[14] H. W. F. Yeung, J. Hou, X. Chen, J. Chen, Z. Chen, and Y. Y. Chung, "Light field spatial super-resolution using deep efficient spatial-angular separable convolution," *IEEE Trans. Image Process.*, vol. 28, no. 5, pp. 2319–2330, May 2019.

[15] J. Jin, J. Hou, J. Chen, and S. Kwong, "Light field spatial super-resolution via deep combinatorial geometry embedding and structural consistency regularization," in *Proc. IEEE Conf. Comput. Vis. Pattern Recognit. (CVPR)*, Jun. 2020, pp. 2260–2269.

[16] S. Zhang, S. Chang, and Y. Lin, "End-to-end light field spatial super-resolution network using multiple epipolar geometry," *IEEE Trans. Image Process.*, vol. 30, pp. 5956–5968, 2021.

[17] Z. Cheng, Z. Xiong, and D. Liu, "Light field super-resolution by jointly exploiting internal and external similarities," *IEEE Trans. Circuits Syst. Video Technol.*, vol. 30, no. 8, pp. 2604–2616, Aug. 2019.

[18] Y. Wang, J. Yang, L. Wang, X. Ying, T. Wu, W. An, and Y. Guo, "Light field image super-resolution using deformable convolution," *IEEE Trans. Image Process.*, vol. 30, pp. 1057–1071, Dec. 2020.

[19] J. Jin, M. Guo, J. Hou, H. Liu, and H. Xiong, "Light field reconstruction via deep adaptive fusion of hybrid lenses," *IEEE Trans. Pattern Anal. Mach. Intell.*, vol. 45, no. 10, pp. 12 050–12 067, 2023.

[20] G. Liu, H. Yue, J. Wu, and J. Yang, "Intra-inter view interaction network for light field image super-resolution," *IEEE Trans. Multimedia*, vol. 25, pp. 256–266, Nov. 2021.

[21] Y. Liu, Z. Cheng, Z. Xiao, and Z. Xiong, "Light field super-resolution using decoupled selective matching," *IEEE Trans. Circuits Syst. Video Technol.*, vol. 34, no. 5, pp. 3313–3326, May 2023.

[22] M. Zhao, H. Sheng, R. Chen, R. Cong, Z. Cui, and D. Yang, "Unelf: Unconstrained neural light field for self-supervised angular super-resolution," *IEEE Trans. Circuits Syst. Video Technol.*, 2025.

[23] M. Guo, J. Hou, J. Jin, J. Chen, and L.-P. Chau, "Deep spatial-angular regularization for light field imaging, denoising, and super-resolution," *IEEE Trans. Pattern Anal. Mach. Intell.*, vol. 44, no. 10, pp. 6094–6110, 2021.

[24] X. Lyu and J. Hou, "Probabilistic-based feature embedding of 4-d light fields for compressive imaging and denoising," *Int. J. Comput. Vis.*, vol. 132, no. 6, pp. 2255–2275, 2024.

[25] K. Ko, Y. J. Koh, S. Chang, and C.-S. Kim, "Light field super-resolution via adaptive feature remixing," *IEEE Trans. Image Process.*, vol. 30, pp. 4114–4128, 2021.

[26] Z. Cheng, Y. Liu, and Z. Xiong, "Spatial-angular versatile convolution for light field reconstruction," *IEEE Trans. Comput. Imag.*, vol. 8, pp. 1131–1144, 2022.

[27] Y. Mo, Y. Wang, C. Xiao, J. Yang, and W. An, "Dense dual-attention network for light field image super-resolution," *IEEE Trans. Circuits Syst. Video Technol.*, vol. 32, no. 7, pp. 4431–4443, Jul. 2022.

[28] V. Van Duong, T. N. Huu, J. Yim, and B. Jeon, "Light field image super-resolution network via joint spatial-angular and epipolar information," *IEEE Trans. Comput. Imag.*, vol. 9, pp. 350–366, 2023.

[29] Z. Liang, Y. Wang, L. Wang, J. Yang, and S. Zhou, "Light field image super-resolution with transformers," *IEEE Signal Process. Lett.*, vol. 29, pp. 563–567, 2022.

[30] S. Wang, T. Zhou, Y. Lu, and H. Di, "Detail-preserving transformer for light field image super-resolution," in *Proc. AAAI Conf. Artif. Intell.*, 2022, pp. 1–9.

[31] R. Cong, H. Sheng, D. Yang, Z. Cui, and R. Chen, "Exploiting spatial and angular correlations with deep efficient transformers for light field image super-resolution," *IEEE Trans. Multimedia*, vol. 26, pp. 1421–1435, Jun. 2023.

[32] Z. Liang, Y. Wang, L. Wang, J. Yang, S. Zhou, and Y. Guo, "Learning non-local spatial-angular correlation for light field image super-resolution," in *Proc. IEEE Int. Conf. Comput. Vis. (ICCV)*, 2023, pp. 12 376–12 386.

[33] A. Gu and T. Dao, "Mamba: Linear-time sequence modeling with selective state spaces," *arXiv:2312.00752*, 2023.

[34] R. Gao, Z. Xiao, and Z. Xiong, "Mamba-based light field super-resolution with efficient subspace scanning," in *Proc. Asian Conf. Comput. Vis. (ACCV)*, 2024, pp. 531–547.

[35] W. Xia *et al.*, "Lfmamba: Light field image super-resolution with state space model," *arXiv:2406.12463*, 2024.

[36] L. Zhu, B. Liao, Q. Zhang, X. Wang, W. Liu, and X. Wang, "Vision mamba: Efficient visual representation learning with bidirectional state space model," *arXiv:2401.09417*, 2024.

[37] Y. Liu, Y. Tian, Y. Zhao, H. Yu, L. Xie, Y. Wang, Q. Ye, J. Jiao, and Y. Liu, "Vmamba: Visual state space model," in *NeurIPS*, 2024.

[38] M. Levoy and P. Hanrahan, "Light field rendering," in *Seminal Graphics Papers: Pushing the Boundaries, Volume 2*, 2023, pp. 441–452.

[39] Y. Wang, L. Wang, J. Yang, W. An, J. Yu, and Y. Guo, "Spatial-angular interaction for light field image super-resolution," in *Proc. Eur. Conf. Comput. Vis.* Cham, Switzerland: Springer, 2020, pp. 290–308.

[40] Y. Wang, L. Wang, G. Wu, J. Yang, W. An, J. Yu, and Y. Guo, "Disentangling light fields for super-resolution and disparity estimation," *IEEE Trans. Pattern Anal. Mach. Intell.*, vol. 45, no. 1, pp. 425–443, Jan. 2023.

[41] M. Guo, J. Hou, J. Jin, H. Liu, H. Zeng, and J. Lu, "Content-aware warping for view synthesis," *IEEE Trans. Pattern Anal. Mach. Intell.*, vol. 45, no. 8, pp. 9486–9503, 2023.

[42] X. Lyu, Z. Zhu, M. Guo, J. Jin, J. Hou, and H. Zeng, "Learning spatial-angular fusion for compressive light field imaging in a cycle-consistent framework," in *Proc. ACM Int. Conf. Multimedia (ACM MM)*, 2021, pp. 4613–4621.

[43] J. Jin, J. Hou, J. Chen, H. Zeng, S. Kwong, and J. Yu, "Deep coarse-to-fine dense light field reconstruction with flexible sampling and geometry-aware fusion," *IEEE Trans. Pattern Anal. Mach. Intell. (TPAMI)*, vol. 44, no. 4, pp. 1819–1836, 2020.

[44] Z. Xiao and Z. Xiong, "Incorporating degradation estimation in light field spatial super-resolution," *Comput. Vis. Image Underst. (CVIU)*, vol. 252, p. 104295, 2025.

[45] Z. Xiao, Z. Li, and W. Jia, "Occlusion-embedded hybrid transformer for light field super-resolution," in *Proc. AAAI Conf. Artif. Intell. (AAAI)*, vol. 39, no. 8, 2025, pp. 8700–8708.

[46] Z. Xiao, Y. Liu, R. Gao, and Z. Xiong, "Cutmib: Boosting light field super-resolution via multi-view image blending," in *Proc. IEEE/CVF Conf. Comput. Vis. Pattern Recognit. (CVPR)*, 2023, pp. 1672–1682.

[47] R. E. Kalman, "A new approach to linear filtering and prediction problems," *J. Basic Eng.*, vol. 82, no. 1, Mar. 1960.

[48] A. Gu, K. Goel, and C. Ré, "Efficiently modeling long sequences with structured state spaces," *arXiv:2111.00396*, 2021.

[49] J. T. Smith, A. Warrington, and S. W. Linderman, "Simplified state space layers for sequence modeling," *arXiv:2208.04933*, 2022.

[50] D. Y. Fu, T. Dao, K. K. Saab, A. W. Thomas, A. Rudra, and C. Ré, "Hungry hungry hippos: Towards language modeling with state space models," *arXiv:2212.14052*, 2022.

[51] Z. Xing, T. Ye, Y. Yang, G. Liu, and L. Zhu, "Segmamba: Long-range sequential modeling mamba for 3d medical image segmentation," in *International Conference on Medical Image Computing and Computer-Assisted Intervention*. Springer, 2024, pp. 578–588.

[52] K. Li, X. Li, Y. Wang, Y. He, Y. Wang, L. Wang, and Y. Qiao, "Videomamba: State space model for efficient video understanding," in *Proc. Eur. Conf. Comput. Vis. (ECCV)*. Springer, 2024, pp. 237–255.

[53] G. Chen, Y. Huang, J. Xu, B. Pei, Z. Chen, Z. Li, J. Wang, K. Li, T. Lu, and L. Wang, "Video mamba suite: State space model as a versatile alternative for video understanding," *arXiv:2403.09626*, 2024.

[54] D. Liang, X. Zhou, W. Xu, X. Zhu, Z. Zou, X. Ye, X. Tan, and X. Bai, "Pointmamba: A simple state space model for point cloud analysis," *arXiv:2402.10739*, 2024.

[55] X. Han, Y. Tang, Z. Wang, and X. Li, "Mamba3d: Enhancing local features for 3d point cloud analysis via state space model," in *Proceedings of the 32nd ACM International Conference on Multimedia*, 2024, pp. 4995–5004.

[56] K. Jin, Z. Wei, A. Yang, D. Wu, M. Gao, and X. Zhou, "Lftransmamba: A hybrid mamba-transformer model for light field image super-resolution," in *Proc. IEEE/CVF Conf. Comput. Vis. Pattern Recognit. (CVPR)*, 2025, pp. 1195–1204.

[57] H. Guo, J. Li, T. Dai, Z. Ouyang, X. Ren, and S.-T. Xia, "Mambair: A simple baseline for image restoration with state-space model," in *Proc. Eur. Conf. Comput. Vis. (ECCV)*. Springer, 2024, pp. 222–241.

[58] B. Lim, S. Son, H. Kim, S. Nah, and K. Mu Lee, "Enhanced deep residual networks for single image super-resolution," in *Proc. IEEE Conf. Comput. Vis. Pattern Recognit. Workshops*, 2017, pp. 136–144.

[59] Y. Zhang, K. Li, K. Li, L. Wang, B. Zhong, and Y. Fu, "Image super-resolution using very deep residual channel attention networks," in *Proc. Eur. Conf. Comput. Vis. (ECCV)*, 2018, pp. 286–301.

[60] A. Dosovitskiy, "An image is worth 16x16 words: Transformers for image recognition at scale," *ICLR*, 2021.

[61] M. Rerabek and T. Ebrahimi, "New light field image dataset," in *Proc. 8th Int. Conf. Qual. Multimedia Exp.*, 2016, pp. 1–2.

[62] S. Wanner, S. Meister, and B. Goldluecke, "Datasets and benchmarks for densely sampled 4d light fields." in *VMV*, vol. 13, 2013, pp. 225–226.

[63] K. Honauer, O. Johannsen, D. Kondermann, and B. Goldluecke, "A dataset and evaluation methodology for depth estimation on 4d light fields," in *Proc. Asian Conf. Comput. Vis. (ACCV)*. Springer, 2017, pp. 19–34.

[64] M. Le Pendu, X. Jiang, and C. Guillemot, "Light field inpainting propagation via low rank matrix completion," *IEEE Trans. Image Process.*, vol. 27, no. 4, pp. 1981–1993, Apr. 2018.

[65] V. Vaish and A. Adams, "The (new) stanford light field archive," *Comput. Graph. Lab., Stanford Univ.*, vol. 6, no. 7, 2008.

[66] S. Zhang, H. Sheng, C. Li, J. Zhang, and Z. Xiong, "Robust depth estimation for light field via spinning parallelogram operator," *Comput. Vis. Image Understand.*, vol. 145, pp. 148–159, Apr. 2016.

Haosong Liu received the B.E. degree from the School of Information Science and Engineering, Huaqiao University, Xiamen, China, in 2023. He is currently pursuing the M.S. degree in Information and Communication Engineering with the School of Information Science and Engineering, Huaqiao University, Xiamen, China. His research interests include light field image restoration and deep learning.

Xiancheng Zhu received the M.S. degree in computer technology from Huaqiao University, Quanzhou, China, in 2023. He is currently pursuing the Ph.D. degree in intelligent manufacturing engineering at the School of Mechanical Engineering and Automation, Huaqiao University. His research interests include image restoration, industrial image super-resolution, and deep learning.

Huanqiang Zeng (Senior Member, IEEE) received the B.S. and M.S. degrees in electrical engineering from Huaqiao University, China, and the Ph.D. degree in electrical engineering from Nanyang Technological University, Singapore.

He is currently a Full Professor of Huaqiao University and Xiamen University of Technology. Before that, he was a Postdoctoral Fellow at The Chinese University of Hong Kong, Hong Kong. He has published more than 190 papers in well-known journals and conferences, including three best poster/paper awards (in the International Forum of Digital TV and Multimedia Communication 2018 and the Chinese Conference on Signal Processing 2017/2019). His research interests include image processing, video coding, machine learning, and computer vision. He has also been actively serving as the General Co-Chair for IEEE International Symposium on Intelligent Signal Processing and Communication Systems 2017 (ISPACS2017), the Co-Organizer for ICME2020 Workshop on 3D Point Cloud Processing, Analysis, Compression, and Communication, the Technical Program Co-Chair for Asia–Pacific Signal and Information Processing Association Annual Summit and Conference 2017 (APSIPA-ASC2017), the Area Chair for IEEE International Conference on Visual Communications and Image Processing (VCIP2015 and VCIP2020), and a technical program committee member for multiple flagship international conferences. He has been actively serving as an Associate Editor for IEEE Transactions on Image Processing, IEEE Transactions on Circuits and Systems for Video Technology, and IET Electronics Letters, and a Senior Area Editor for IEEE Signal Processing Letters.

Jianqing Zhu (Senior Member, IEEE)received the B.S. degree in Communication Engineering and the M.S. degree in Communication and Information System from the School of Information Science and Engineering, Huaqiao University, Xiamen, China, in 2009 and 2012, respectively. He received the Ph.D. degree in Computer Application Technology from the Institute of Automation, Chinese Academy of Sciences, Beijing, China, in 2015. He is now a Professor at the College of Engineering, Huaqiao University, Quanzhou, China. His current research interests include computer vision and pattern recognition, with a focus on image and video analysis, particularly person re-identification, object detection, and video surveillance. He was awarded the Best Biometrics Student Paper award at the International Conference on Biometrics in 2015.

Jiuwen Cao (Senior Member, IEEE) received the B.Sc. and M.Sc. degrees from the School of Applied Mathematics, University of Electronic Science and Technology of China, Chengdu, China, in 2005 and 2008, respectively, and the Ph.D. degree from the School of Electrical and Electronic Engineering, Nanyang Technological University (NTU), Singapore, in 2013. From 2012 to 2013, he was a Research Fellow at NTU. He is currently a Professor and Vice Dean of the School of Automation at Hangzhou Dianzi University, Hangzhou, China. His main research interests include machine learning, neural networks, and medical signal processing. He has published over 180 papers in top-tier journals and conferences and has been awarded the Best Conference Paper of ICCSIP 2020 and the Best Conference Paper Finalist of ICCSIP 2021. He is an Associate Editor of IEEE Transactions on Circuits and Systems—I: Regular Paper, The Journal of the Franklin Institute, Neurocomputing, Military Medical Research, and Multidimensional Systems and Signal Processing.

Junhui Hou is an Associate Professor with the Department of Computer Science, City University of Hong Kong. He holds a B.Eng. degree in information engineering (Talented Students Program) from the South China University of Technology, Guangzhou, China, an M.Eng. degree in signal and information processing from Northwestern Polytechnical University, Xi'an, China, and a Ph.D. degree from the School of Electrical and Electronic Engineering, Nanyang Technological University, Singapore. His research interests are neural spatial computing.

Dr. Hou received the Early Career Award (3/381) from the Hong Kong Research Grants Council in 2018 and the NSFC Excellent Young Scientists Fund in 2024. He has served or is serving as an Associate Editor for *IEEE Transactions on Visualization and Computer Graphics*, *IEEE Transactions on Image Processing*, *IEEE Transactions on Multimedia*, and *IEEE Transactions on Circuits and Systems for Video Technology*.